Revision 2

Hydrogen incorporation and the oxidation state of iron in ringwoodite – a spectroscopic study

Maria Mrosko[1], Stephan Lenz[2], Catherine A McCammon[3], Michail Taran[4], Richard Wirth[1], Monika Koch-Mueller[1]

[1]Chemistry and Physics of Earth Materials, GFZ Potsdam, Potsdam, Germany. Email: mrosko@gfz-potsdam.de

[2]Institute for Applied Geosciences, Technical University Berlin, Berlin, Germany.

[3]Bayerisches Geoinstitut, University of Bayreuth, Bayreuth, Germany.

[4]Institute of Geochemistry, Mineralogy and Ore Formation, National Academy of Sciences of Ukraine, Kiev, Ukraine.

Abstract

We conducted several multi-anvil-experiments to synthesize iron-bearing ($0.11 \leq x_{Fe} \leq 0.24$) hydrous ringwoodite under oxidizing and reducing conditions. The experiments were performed at 1200 °C and pressures between 16.5 and 18.3 GPa. The incorporation of hydrogen and iron in ringwoodite was studied using FTIR, MB, UV-VIS and EEL spectroscopy. For MB spectroscopy, ringwoodite enriched in ^{57}Fe was synthesized. The IR spectra of ringwoodite show a broad OH band around 3150 cm^{-1} and two shoulders on the high-energy side: one intense at 3680 cm^{-1} and one weak at around 3420 cm^{-1}. The water content of the samples was determined using FTIR spectroscopy to have a maximum value of 1.9 (3) wt% H_2O. UV-VIS spectra display a broad band around 12700 cm^{-1} and a shoulder at 9900 cm^{-1} representing the spin allowed dd-transitions of $^{VI}Fe^{2+}$. The weaker band around 18200 cm^{-1} is a distinct feature of Fe^{2+} - Fe^{3+} intervalence charge transfer indicating the

presence of Fe^{3+} in the samples. EEL spectra yield Fe^{3+} fractions ranging from 6 (3) at reducing conditions to 12 (3) % at oxidizing conditions.

We performed heating experiments up to 600 °C in combination with *in situ* FTIR spectroscopy to evaluate the temperature dependent behavior of ringwoodite, especially with respect to hydrogen incorporation. We observed a color change of ringwoodite from blue to green to brown. The heat treated samples displayed hydrogen loss, an irreversible rearrangement of part of the hydrogen atoms (FTIR), as well as oxidation of Fe^{2+} to Fe^{3+} evidenced by the appearance of the spin forbidden dd-transition band for Fe^{3+} and the ligand-metal (O^{2-} - Fe^{3+}) transition band in the optical spectra. An increased Fe^{3+} fraction was also revealed by EEL and MB spectroscopy (up to 16 % $Fe^{3+}/\Sigma Fe$). Analyses of MB data revealed the possibility of tetrahedral Fe^{3+} in the annealed ringwoodite.

These results lead to a reinterpretation of the broad OH band, which is a combination of several bands, mainly $[V_{Mg}(OH)_2]^x$), a weaker high-energy band at 3680 cm^{-1} ($[V_{Si}(OH)_4]^x$) and a shoulder at 3420 cm^{-1} ($[(Mg/Fe)_{Si}(OH)_2]^x$).

Keywords: ringwoodite, water, iron, oxygen fugacity, hydrogen location, spectroscopy

Introduction

Ringwoodite is the most abundant mineral in the lower part of the transition zone in the Earth's mantle. The transition from the orthorhombic β-polymorph (wadsleyite) to the high-pressure γ-polymorph of $(Mg,Fe)_2SiO_4$ (ringwoodite) is believed to cause the discontinuity in seismic wave velocity at 520 km depth, where ringwoodite has the cubic spinel structure with space group $Fd\bar{3}m$. Ringwoodite belongs to the group of nominally anhydrous minerals, but can incorporate up to 2.5 wt% water as OH^- via point defects (e.g. Kohlstedt et al. 1996; Kudoh et al. 2000). The location of hydrogen within the structure is still an object of diverse discussion, since the cubic structure of ringwoodite becomes more complex as shown for

example by polarized Fourier transform infrared (FTIR) spectroscopy. Kudoh et al. (2000) proposed that the broad IR-active band around 3165 cm^{-1} indicates the location of hydrogen atoms between O-O pairs of the 16c (vacant) and the 16d (partially vacant) octahedral sites. In contrast, Smyth et al. (2003) and Chamorro et al. (2006) assigned that broad band to protonation of tetrahedral edges. The latter authors also stated that the smaller high-energy band at 3679 cm^{-1} is caused by hydrogen located at octahedral edges. The above mentioned studies all indicate octahedral vacancies and Mg-Si disorder as potential charge balancing mechanisms for the hydrogen incorporation. Blanchard et al. (2009) likewise support the idea of OH defects associated not only with octahedral vacancies but also with partial cationic inversion of the structure. Based on a first-principles study they assigned the broad OH-band to protonation of octahedral edges (similar to Kudoh et al. 2000) and suggested a hydrogarnet-type defect for the smaller band at app. 3675 cm^{-1}.

The question of where hydrogen atoms are located in the structure becomes more complex when iron is present in the system, because additional factors such as iron oxidation state and thus oxygen fugacity have to be taken into consideration. Naturally occurring ringwoodite contains an assumed amount of about 11 % Fe (Kleppe et al. 2002). The presence of iron in two oxidation states (Fe^{2+} and Fe^{3+}) increases the number of possible protonation sites, for example when Fe^{3+} is reduced to Fe^{2+} in the course of OH group formation (Kleppe et al. 2002; Ingrin and Skogby 2000).

While the oxidation state of iron in ringwoodite and the incorporation of water are each interesting issues themselves, the mutual interaction of both mechanisms is even more complex, but needs to be studied in order to understand mantle behavior and processes, as performed for example by McCammon et al. (2004) for the mantle minerals olivine, wadsleyite, ringwoodite and majorite.

The method of choice for this kind of investigation, in which minor elements and species and their local environment are of interest, is spectroscopy. The present study focuses on the

incorporation of OH^-, Fe^{2+} and Fe^{3+} and their mutual interaction by applying FTIR, Mössbauer (MB), electron energy loss (EEL), and UV-VIS spectroscopy. Furthermore, we combined these spectroscopic measurements with heating experiments both *in situ* and *ex situ* to evaluate the response of the structure and species to temperature and thus obtain further insight into their structural location and correlation with each other.

Experimental and analytical methods

Syntheses

Multi-anvil apparatus.

The high-pressure syntheses of wadsleyite were performed in a multi-anvil apparatus similar to that of Walker (1991), but with a special tool that allows alternatively a continuous 360° rotation or a 180° rocking motion of the Walker high-pressure module during the run with 5° s^{-1} in order to avoid separation of the fluid from the solid parts of the run and thus ensure a homogeneous starting material (see Schmidt and Ulmer 2004; Deon et al. 2010). We used a 10/5-assembly (octahedron length/truncation length) with an MgO-based octahedron serving as the pressure-transmitting medium, a stepped graphite heater and pyrophyllite gaskets. The temperature was controlled by a W5%Re-W26%Re thermocouple. Details of the experimental set up are given in Koch-Müller et al. (2009).

Oxide mixtures of different composition served as starting materials for the syntheses and were filled into Pt capsules (length 1.78 mm, outer diameter 2.54 mm). Run MA327 contained ^{57}Fe-enriched Fe_2O_3 (Fe 90% enriched) as an iron oxide component for later MB spectroscopy.

Oxygen fugacity in runs MA311 and MA327 was set to oxidizing conditions by adding Re/ReO_2 to the starting material, while Run MA313 was performed under more reducing conditions by adding Fe/FeO in a separate (but hydrogen permeable) part of the sample capsule. In all runs an amount of 0.4 mg (4 wt%) distilled water was first filled into the

capsule before adding the starting material, and the filled capsule was then cold-sealed. The experimental conditions are summarized in Table 1.

Analyses

FTIR spectroscopy.

OH-absorption spectra were measured using a VERTEX 80v FTIR spectrometer (Bruker Optics) with an attached Hyperion microscope. A globar served as a light source, and further devices were an InSb detector and a KBr beam splitter. The spectra were collected in a range from 6000 to 2000 cm^{-1} with a resolution of 2 cm^{-1} and averaged over 256 scans. We performed measurements for quantification purposes on doubly polished crystal plates of known thickness.

The integral intensities of the OH-bands were obtained using the PeakFit software by Jandel Scientific. We applied a Gaussian plus Lorentzian distribution function to all component bands. Water contents were calculated using the formula

$$c\ (wt\%\ H_2O) = A_i\ (cm^{-1}) * 1.8/[t\ (cm) * D\ (g/cm^3) * \varepsilon_i\ (l*mol^{-1}*cm^{-2})]$$

where A_i is the total integral intensity of bands, D is the density, t is the thickness of the sample and ε_i is the integral molar absorption coefficient of ringwoodite = 100000 +/- 10000 $l*mol^{-1}*cm^{-2}$ (Koch-Müller and Rhede 2010). Since ringwoodite is isotropic the total integral intensities were calculated by multiplying the integrated area of the bands by three.

To investigate the temperature-dependence of OH-bands, we collected spectra up to 600 °C in a Linkam FTIR600 heating/cooling stage with N_2- and air flushing, respectively. Temperature was increased in steps of 100 °C and each measurement was started after an annealing time of about 20 minutes.

EEL spectroscopy.

130 The ferric iron to total iron ratio of the samples was determined by EEL spectroscopy.
131 Therefore thin foils (thickness should not exceed 100 nm) were cut from polished single
132 crystals using a FEI FIB200 focused ion beam device (Wirth 2004), with a Ga-ion source
133 operated at an acceleration voltage of 30 kV. The final transmission electron transparent foil
134 was removed from the sample with an *ex situ*-manipulator and placed onto a perforated
135 transmission electron microscope (TEM) carbon grid. No further carbon coating was required.
136 Analyses were performed with a FEI Tecnai G2 F20 X-Twin TEM operating at 200 kV with a
137 field emission gun (FEG) electron source and a Gatan Tridiem energy filter with an energy
138 resolution of 1 eV. The EEL spectra were acquired in the diffraction mode with a camera
139 length of 770 mm and a collection angle of 10 mrad. They were averaged over 5 scans, with 1
140 second acquisition time each. The spot size was 5 nm, and we measured about 10 different
141 locations in each foil.

142 The determination of $Fe^{3+}/\Sigma Fe$ was carried out applying the technique of the modified
143 integral Fe L_{23} white-line intensity ratio (van Aken and Liebscher 2002). As per their
144 description, the background was fitted to a double arctan function with its height scaled to the
145 minima behind the Fe L_3- and L_2-edges and fixed inflection points at 708.65 and 721.65 eV.
146 After subtracting the background, two integration windows of 2 eV width each were
147 positioned around 709.5 and 720.7 eV for L_3Fe^{3+} and L_2Fe^{2+}, respectively. The final $Fe^{3+}/\Sigma Fe$
148 ratios were calculated applying the following calibration curve (with a = 0.193 (7), b = - 0.465
149 (9), c = 0.366 (3))

150 $$\frac{I(L_3)}{I(L_2)_{\mathrm{mod}}} = \frac{1}{ax^2 + bx + c} - 1.$$

151 The background subtraction and determination of $Fe^{3+}/\Sigma Fe$ ratios were performed using a
152 program written by C. Petrick (Helmholtz-Zentrum Potsdam, Deutsches
153 GeoForschungsZentrum - GFZ, Potsdam, Germany).
154

MB spectroscopy.

MB spectra were recorded at room temperature (293 K) in transmission mode on a constant acceleration MB spectrometer with a nominal 370 MBq ^{57}Co high specific activity source in a 12 μm thick Rh matrix. The velocity scale was calibrated relative to 25 μm thick α-Fe foil using the positions certified for (former) National Bureau of Standards standard reference material no. 1541; line widths of 0.36 mm/s for the outer lines of α-Fe were obtained at room temperature. For the measurements, a grain of each sample was embedded in a small amount of Apiezon grease and then crushed between two glass slides. The material was removed using cellophane tape, which was then placed over a piece of mylar. Subsequently, a piece of 25 μm thick Ta foil (absorbs 99% of 14.4 keV gamma rays) with a hole of 250 - 300 μm diameter was centered over the sample powder.

Based on sample composition, iron enrichment and estimated physical thickness, the dimensionless thickness of the samples was estimated to be roughly 8, which corresponds to about 20 mg Fe (unenriched)/cm^2. Data were fitted using the fitting program MossA written by C. Prescher (Prescher et al. 2012).

UV-VIS spectroscopy.

Optical absorption spectra were measured in the range from 370 to 1800 nm (ca. 27000 - 5555 cm^{-1}) with a single-beam micro spectrophotometer constructed based on a SpectraPro-275 triple grating monochromator, a highly modified mineralogical microscope MIN-8 and a PC. Ultrafluars (10×) serve as objective and condenser. Two exchangeable highly stabilized quartz-halogen and Xenon lamps (70 W each) are used as a light source. Two exchangeable photomultiplier tubes and a cooled PbS-cell act as photo detectors. A mechanical high-stabilized 300 Hz-chopper and a lock-in amplifier were applied to improve the signal/noise ratio. The spectra were scanned in steps of $\Delta\lambda$ = 1 nm, 2 nm and 5 nm in the range of 270-450, 450-1000 and 1000-1800 nm, respectively. The spot size was 100 μm maximum.

The samples of synthetic ringwoodite were prepared as thin sections of about 50 μm thickness. For this purpose, optically homogeneous grains of ringwoodite were glued with epoxy on a supporting glass plate and doubly polished with diamond powders and pastes until transparent thin sections were obtained that were suitable for optical spectroscopic measurements. Optical absorption spectra of the thin sections were measured at ambient conditions. The reference beam position was always taken on a supporting glass plate near to where the thin section was measured.

Electron microprobe analysis (EMPA).

For chemical analyses, several ringwoodite single crystals (MA327 and MA311) and one half of a cut sample capsule (run MA313) were embedded in epoxy, polished and coated with carbon. Compositions were measured with a JEOL JXA-8500F electron microprobe using wavelength-dispersive spectrometers with a PAP correction procedure. The microprobe was operated at 15 kV with a beam current of 10 nA and a spot size of 2 μm. Counting times were 20 s on peak and 10 s on the background. A well-characterized ringwoodite (MA056) served as a standard.

Single crystal X-ray diffraction (XRD).

The lattice parameters of the ringwoodite crystals were determined using a Rigaku R/AXIS-SPIDER diffractometer operating at 40 kV and 30 mA. A rotating Cu anode served as the source where the emitted light is directed through an arrangement of mirrors to yield monochromatic Cu$K\alpha$ radiation. The detection system consists of a cylindrically shaped image plate, which reads out the diffracted radiation in a 2θ range of – 60 to 144° in horizontal and +/- 45° in vertical direction. The program RAPID/XRD Rigaku was used for data acquisition with an exposure time of 10 min. Data treatment was performed using the software AreaMax – Rigaku/MSC.

Results

Ringwoodite after synthesis

The synthesized ringwoodite crystals were xenomorphically shaped and their size ranged from 20 to 200 μm. Their color varied from light blue (MA313 with $x_{Fe} = 0.11$) to darker blue (MA311 and MA327 with $x_{Fe} = 0.18$ and 0.24, respectively) with increasing Fe-content. In all samples a silicon deficit was observed with x_{Si} ranging between 0.95 and 0.97. The amount of incorporated water was determined to a maximum value of 1.9 (3) wt% H_2O in MA313. EEL spectroscopy revealed the ferric iron contents (relative to total iron) to be 6 (3) % in the more reduced runs and up to 12 (3) % in the experiments under more oxidized conditions. See Table 1 for detailed information for each run. Based on EMP analyses, calculated water contents and Fe^{3+} fractions (values taken from EELS) we determined the following stoichiometric formulae:

$(Mg_{0.79(2)}Fe^{2+}_{0.16(1)}Fe^{3+}_{0.02(1)})_2Si_{0.97(4)}H_{0.20(4)}O_4$ (MA311),

$(Mg_{0.86(1)}Fe^{2+}_{0.10(1)}Fe^{3+}_{0.01(1)})_2Si_{0.95(1)}H_{0.31(4)}O_4$ (MA313) and

$(Mg_{0.76(1)}Fe^{2+}_{0.21(1)}Fe^{3+}_{0.03(1)})_2Si_{0.95(1)}H_{0.15(4)}O_4$ (MA327).

The MB spectrum of the original ringwoodite crystal was fitted to one Fe^{2+} and one Fe^{3+} doublet. The Fe^{2+} doublet displays large center shift (1.069 mm/s relative to α-Fe) and quadrupole splitting (2.767 mm/s) that is consistent with octahedral coordination for Fe^{2+}. The other doublet with low center shift (0.665 mm/s) and quadrupole splitting (1.063 mm/s) is assigned to octahedral Fe^{3+}, resulting in 9 (3) % of ferric iron. Table 2 lists the MB data and assignments resulting from the fitting process.

Heating experiments

FTIR spectroscopy.

We performed several heating experiments on crystals from runs MA313 and MA327 to a maximum temperature of 600 °C and performed *in situ* FTIR spectroscopy. For the purpose of comparison we additionally investigated a ringwoodite sample of magnesium endmember composition (MA308) and other iron-bearing ringwoodites in order to evaluate the effect of iron on the OH band structure of original and annealed ringwoodite.

The most striking observation was a color change of the crystals from the original blue to green starting at about 300 °C, which was non-reversible upon cooling (see Figure 1). The color modification was accompanied by a dramatic change in the infrared spectrum between 4000 and 2000 cm^{-1} where the OH stretching bands occur. Figure 2 displays the absorbance spectra of MA313 ringwoodite at ambient conditions, *in situ* at 500 °C and after quenching to room temperature. There are four main changes in the spectra:

(1) The high energy OH stretching band at 3680 cm^{-1} is strongly enhanced during heating and displays a slight irreversible shift to lower wavenumbers.

(2) The shoulder at 3420 cm^{-1} is only weakly pronounced in the spectrum at ambient conditions but increases strongly at 500 °C.

(3) In contrast, the broad stretching band around 3150 cm^{-1} shows a distinct decrease during heating.

(4) The band group around 2500 cm^{-1} vanishes almost completely at 500 °C, but returns once the sample is cooled down to room temperature.

Except for the last mentioned change, all modifications are non-reversible and therefore visible in the spectrum after quenching. Apart from the obvious rearrangement of the OH stretching bands, the ringwoodite loses about 30 % of its initial water content due to heating.

We performed the experiments both under rather oxidizing (air-flushing) and more or less inert (N_2-flushing) conditions and observed no differences with respect to the appearance of the spectra or calculated water contents. The annealed crystals were checked by Raman spectroscopy and still showed the signature of ringwoodite.

258

259 **UV-VIS spectroscopy.**

260 Figure 3 shows the optical absorption spectra of sample MA313 of the original crystal (blue
261 curve, ambient), and the 500 °C - (green, 500 °C) and the 600 °C - annealed crystals (orange,
262 600 °C). The blue curve of the original crystal shows the spin-allowed dd-transition band of
263 octahedral Fe^{2+} at 12700 cm^{-1} with a smaller shoulder at 9900 cm^{-1}. The second important
264 feature is the intervalence charge transfer band (IVCT) of Fe^{2+}/Fe^{3+} at about 18200 cm^{-1}.
265 Compared to the original spectrum, the green curve of the crystal annealed at 500 °C displays
266 three characteristic modifications: a strong decrease of the spin-allowed transition bands of
267 octahedral Fe^{2+}, a decrease of the IVCT band and the appearance of a band at 21400 cm^{-1},
268 which is assigned to a spin-forbidden transition of Fe^{3+}. This band is further enhanced in the
269 600 °C-treated sample, in which, likewise, the low-energy edge of the ligand-metal transition
270 band of $O^{2-} \rightarrow Fe^{3+}$ is visible.

271

272 **Determination of Fe^{3+}.**

273 EEL spectroscopy on all treated samples showed an increase of the ferric iron content due to
274 heating to more or less the same percentage of approximately 16 % $Fe^{3+}/\Sigma Fe$. In sample
275 MA313 a larger fraction of Fe^{2+} is oxidized to Fe^{3+} (6 % $\rightarrow$ 16 %) when compared to the ^{57}Fe
276 enriched sample MA327, in which an increase from 12 to 15 % was determined using EELS
277 (MB spectroscopy revealed an increase from 9 to 11 %).

278 Figure 4 shows the MB spectrum of the annealed ringwoodite with four doublets fit to the
279 data. The two doublets with large center shift (> 1mm/s) and quadrupole splitting are assigned
280 to ferrous iron in octahedral coordination. When compared to the untreated sample, using two
281 Fe^{2+} doublets instead of one gave a better fit, suggesting a slight variation in the next-nearest
282 neighbor environment of Fe^{2+} in octahedral sites. The other two doublets with small center
283 shift (< 1 mm/s) and quadrupole splitting can be assigned to Fe^{3+} in octahedral and possibly

tetrahedral coordination. When we assume Fe^{2+}-Fe^{3+}-charge transfer to be slower than the timescale of the Mössbauer effect, the models give total Fe^{3+} fractions of about 12 % assuming only octahedral Fe^{3+}, and about 11 % assuming both octahedral and tetrahedral Fe^{3+} (9 % octahedral and 2 % tetrahedral Fe^{3+}).

Discussion

In the present study, a maximum water content of 1.9 (3) wt% H_2O is reported in sample MA313 with a Fe^{3+} fraction of 0.06 (3) under reducing conditions. Under increased oxygen fugacity, synthesized ringwoodite contains higher fractions of ferric iron (up to 0.12 (3) in MA327 with 0.8 wt% H_2O). These values are comparable to those in other experimental ringwoodite studies such as McCammon et al. (2004) and Smyth et al. (2003) who reported Fe^{3+} fractions of 0.03 (2) to 0.18 (4) (with the total Fe ranging from 0.2 to 0.3, comparable to the values determined in our study) and water contents up to 2.2 wt% at slightly higher pressure and temperature conditions. These studies also found a silicon deficit ($x_{Si}<1$) in most of their samples. We observed the same behavior in our runs with silicon values for ringwoodite ranging between 0.95 and 0.97. The silicon deficit is most likely a consequence of the incorporation of water.

Our experiments show that incorporation of ferric iron in ringwoodite is strongly influenced by whether synthesis conditions were oxidizing or reducing. For all of our experiments, the amount of Fe^{3+} is higher in the more oxidized runs compared to the reduced experiments. We infer that dissociation of molecular water into H_2 and O_2 and subsequent diffusion of the small H_2 molecule through the permeable Pt capsule walls leads to excess O_2 within the capsule and hence oxidation of ferrous iron.

Correlation between H^+ and Fe^{3+}

On the basis of our analyses of samples with different Fe content, there is no clear correlation between the incorporation of ferric iron and the incorporation of hydrogen as proposed earlier by McCammon et al. (2004), although the mechanism of ferrous iron plus OH^- transforming into $Fe^{3+} + O^{2-} + ½ H_2$ (Ingrin and Skogby 2000) provides a reasonable correlation. But, as described below, the formation of hydrogen defects in ringwoodite is based on more than one mechanism of hydrogen incorporation. Therefore a simple correlation between Fe^{3+} and OH^- is not likely, nor could it be observed in our study. This holds true for the formation of hydrogen defects during the process of crystal growth. In contrast, the heating experiments on different ringwoodite crystals indeed suggest a correlation of dehydration and likewise increasing Fe^{3+} fractions. The annealed crystals lose about 30 % of their initial water content that is coupled to an increased amount of ferric iron. Interestingly, the gain of Fe^{3+} throughout the heating process is highest in the ringwoodite sample with the lowest starting value and vice versa, in such a way that in the end both samples (MA313 and MA327) reach more or less the same fraction of ferric iron. Based on these data and other data in the literature (e.g. Smyth et al. 2003), it seems reasonable to infer a maximum amount for Fe^{3+} incorporation in ringwoodite up to 20 % of the total Fe.

Location of hydrogen

The manner in which the OH bands change during heating provides further insight into the possible location of hydrogen within the ringwoodite structure. The main broad band around 3150 cm^{-1} decreases strongly during heating, characterizing the dehydration, and it most likely is responsible for up to 30 % of the initial amount of water that is lost during heating (see Fig. 2). Simultaneously the ferric iron content is increased throughout the heating process following the relation

$Fe^{2+} + OH^- = Fe^{3+} + O^{2-} + ½ H_2$ (Ingrin and Skogby 2000).

334 The broad band therefore likely represents more loosely bound hydrogen. Blanchard et al.
335 (2005) calculated the defect binding energies for ringwoodite. These values represent the gain
336 of energy for the system when an isolated OH species is bound to a negatively charged defect.
337 In this way the defects with the largest negative values are expected to be more stable, since
338 they represent the largest energy gain for the structure. According to their calculations the
339 most favored combination of an OH species with a defect is to a vacant tetrahedron with an
340 energy gain of about -15 eV per each hydrogen, followed by hydrogen combining with Mg-
341 substituted tetrahedra (~ -12 eV per H) and lastly, the hydrogen bound to a vacant octahedron
342 (~ -10 eV per H). However, the inverse conclusion would be that by introducing energy to the
343 system, the hydrogen atoms bound to a vacant octahedron represent the least stable
344 configuration and would be released first. The broad band around 3150 cm^{-1} displays a
345 distinct intensity decrease during heating. Thus we assume that the binding mechanism of
346 hydrogen causing that band must be the least stable and it is therefore most likely due to
347 octahedral defects $[V_{Mg}(OH)_2]^x$. The other defects ($[V_{Si}(OH)_4]^x$ and $[Mg_{Si}(OH)_2]^x$) are more
348 stable and could be assigned to the bands that increase during heating. Thus we consider a
349 rearrangement of hydrogen atoms to the more stable configuration of tetrahedral vacancies
350 (hydrogarnet-type) and Mg-substituted tetrahedra. The slightly visible shift of the increased
351 band at 3680 cm^{-1} to lower wavenumbers at 500 °C and after heating (see Fig. 2) represents a
352 side effect of the decreased intensity of the broad absorption band around 3150 cm^{-1}.
353 In addition to the altered shape and visibly shifted maxima in the OH absorption spectra, the
354 band deconvolution plots in Figure 5 also clearly show the rearrangement of the bands. The
355 original ringwoodite spectrum (top) consists of five Gaussian and Lorentzian-shaped
356 functions with the most intense one around 3131 cm^{-1}. The comparison to the bottom plot of
357 the annealed sample shows that the bands at 3446 and 3649 cm^{-1} are significantly enhanced at
358 the expense of the formerly strongest band around 3127 cm^{-1}. Thus the heating process not

359 only leads to the loss of part of the initial water content but also induces a rearrangement of
360 the hydrogen.

361 Comparing IR-spectra of iron-bearing with iron-free ringwoodite supports these findings.
362 Figure 6 clearly shows that the higher the amount of incorporated iron, the closer the bands at
363 3115 cm^{-1} and 3700 cm^{-1} (both values for Mg endmember) move towards each other.
364 Concerning the band at 3115 cm^{-1}, the substitution of iron for magnesium in the octahedral
365 site leads to expansion of the octahedron and thus to increased O-O distances or weaker O …
366 H bonds. According to Libowitzky (1999) this would result in a shift of the band towards
367 higher wavenumbers as is actually observed.

368 For the band around 3700 cm^{-1}, we observe a shift towards lower wavenumbers with
369 increasing Fe content. The assignment of the band to hydrogen atoms bound to a vacant
370 tetrahedron (hydrogarnet-substitution) does not initially appear to relate to the incorporation
371 of iron into the structure. However, since the tetrahedron shares an oxygen with the Fe-
372 substituted octahedron, the expansion of the octahedron would push the oxygen towards the
373 vacant tetrahedron and thus shorten O-O distances. As a consequence of this structure
374 modification, the O … H bonds would become stronger and therefore shift to lower
375 wavenumbers as is indeed observed with increasing iron incorporation. Beyond that, the
376 original location of the band at 3680 cm^{-1} (3700 cm^{-1} in iron-free ringwoodite) is typical for
377 the hydrogarnet-substitution (i.e. Andrut et al. 2002), where 4 hydrogen atoms (H^{+}) substitute
378 for the tetrahedrally coordinated Si^{4+}. The mechanism is associated with the enlargement of
379 the vacant $(OH)_4$-tetrahedra as compared to the smaller SiO_4-tetrahedra (i.e. Armbruster et al.
380 2001) and affects properties including the elasticity and rheology at high pressure (Prewitt
381 and Parise 2000).

382 The shoulder around 3420 cm^{-1} is only weakly developed in the original crystals but
383 becomes the main band in the spectra of the annealed ringwoodite. It is also observed in iron-
384 free ringwoodite (around 3250 cm^{-1}) even though it is poorly visible. As a result of increasing

385 x_{Fe} the shoulder shifts towards higher wavenumbers. Interestingly in the Mg endmember the
386 band is very little or not at all enhanced during heating compared to the iron-bearing
387 ringwoodite. From that we infer a possible assignment of the broad band as caused by two
388 hydrogens bound to a cation-substituted tetrahedron (Mg for silicon). Its strong enhancement
389 in the iron-bearing samples could be an indication of additional tetrahedral Fe^{3+}. In that case
390 one would find only one hydrogen bound to a tetrahedron instead of two due to charge
391 balance.

392 At first glance, the position of the band group around 2500 cm^{-1} is indicative of OH
393 groups with strong hydrogen bonding and distances R(O-H…O) around 2.6 Å (Libowitzky
394 1999). At the same time, it has been assigned to either X-OH bending vibrations (Bolfan-
395 Casanova et al. 2000) or as combination of overtones of Si-O-related vibrations and
396 translations of octahedral and tetrahedral cations (Hofmeister and Mao 2001). Interestingly,
397 the band group is not only found in hydrous but also in anhydrous ringwoodite (Hofmeister
398 and Mao 2001) and thus cannot be related to OH within the structure. Latter authors describe
399 the modes that build up the band group as combinations of ν_3 (Si-O tetrahedral stretch), ν_4
400 (O-Si-O tetrahedral bend), and translations of the octahedral cation and SiO_4 unit (T(M) and
401 T(mix)). Furthermore, they show that all modes (except for ν_3) display a dependence of the
402 composition such that with increasing Mg content the bands shift to higher wavenumbers. We
403 observe exactly the same, when comparing the band group in IR spectra of different Fe
404 content (see Fig. 6): the slight shift of the band group to lower wavenumbers with increasing
405 iron content thus is a consequence of the shift of the contributing fundamental bands between
406 200 and 600 cm^{-1}.
407
408 **Fe in ringwoodite**
409 The expansion of the structure as a result of iron incorporation is linked to increased lattice
410 parameters due to the higher ionic radius of iron compared to magnesium. The same effect is

observed with hydrogen incorporation. The anhydrous magnesium endmember displays the lowest lattice parameter with a = 8.0649 (1) Å (Sasaki et al. 1982); whereas Inoue et al. (1998) determined a for hydrous iron-free ringwoodite (2.2 wt% water revealed by secondary ion mass spectrometry (SIMS)) to be 8.0786 (4) Å. Inoue et al. (2004) and Ye et al. (2009) also reported increased lattice parameters of hydrous versus anhydrous ringwoodite. The lattice parameter of our ringwoodite sample (MA313) with x_{Fe} = 0.11 was determined to be even higher at 8.096 (4) Å. Although our sample contains less water (1.9 wt%) and thus should display less of an increase in lattice parameters, the incorporated iron leads to a higher a-value. The same effect is observed in the annealed ringwoodite samples. XRD data of ringwoodite (MA313) revealed an increase of a from 8.096 (4) Å in the original sample to 8.112 (3) Å in the annealed crystal. As aforementioned, the initial a-value is already high compared to other ringwoodite data due to the high water content of the sample. Inoue et al. (2004) performed high-temperature XRD measurements and determined an increase of a in hydrous ringwoodite (with 2.6 wt% H_2O) from 8.065 (1) Å at ambient conditions to 8.105 (2) Å at 500 °C. They also determined breakdown temperatures around 700 °C for anhydrous ringwoodite and 400 °C for hydrous ringwoodite. Ye et al. (2009) also performed heating experiments up to 646 °C (919 K), and likewise observed a unit-cell expansion with increasing temperature and breakdown temperatures of different iron-free ringwoodite crystals depending on the amount of incorporated water. The sample with the highest water content (2.4 wt% H_2O) broke down at 333 °C (606 K); whereas the ringwoodite with only 0.20 wt% H_2O had been stable up to 638 °C (911 K). The samples in our study maintained a ringwoodite signature at the highest temperature of 600 °C (873 K). Based on that observation we assume a stabilizing effect of iron on the structure of hydrous ringwoodite up to higher temperatures.

The UV-VIS spectrum of the heated crystal also displays indications that argue for the expansion of the structure. The IVCT band around 18200 cm^{-1} responsible for the blue color

437 of ringwoodite (Taran et al. 2009) vanishes and causes the crystal to appear greenish. The
438 mechanism that causes the band is electron hopping in overlapping atomic orbitals between
439 two adjacent Fe^{2+} and Fe^{3+} octahedra. The heating of the sample leads to an expansion of the
440 structure and thus probably to separation of the overlapping orbitals such that electron
441 hopping is no longer possible. The IVCT band vanishes and the crystal takes on a green color.
442 The evolution of the optical absorption spectra during the temperature treatment (see
443 Fig. 3) reflects an oxidation of Fe^{2+} to Fe^{3+}. Indeed, both spectroscopic features related to
444 Fe^{2+}, the Fe^{2+}/Fe^{3+} IVCT band at around 18200 cm^{-1} and, especially, the broad band at
445 ~12700 with a weaker shoulder at ~9900 cm^{-1}, assigned to the electronic spin-allowed dd
446 transition $^5T_{2g} \rightarrow {}^5E_g$ of Fe^{2+}, split by the dynamic Jahn-Teller effect (Taran et al. 2009),
447 continually decrease with increasing temperature (see Fig. 3). This behavior evidently
448 indicates the decrease of Fe^{2+}. On the other hand, there is a significant intensification of the
449 high-energy absorption edge, which is most probably caused by the strong UV absorption
450 induced by the electronic ligand-to-metal charge-transfer transition $O^{2-} \rightarrow Fe^{3+}$. Besides, the
451 shoulder around 22000 cm^{-1}, that very likely may be assigned to the spin-forbidden $^6A_1 \rightarrow$
452 $^4A_1$, ^4E (^4G) transition of Fe^{3+}, appears and considerably increases with temperature. That
453 again indicates an oxidation of Fe^{2+} to Fe^{3+} induced by heating.
454 This is confirmed by EELS and MB analyses that clearly yield increased contents of ferric
455 iron in the annealed ringwoodite crystals.
456 There is still some uncertainty about which sites Fe^{3+} occupies in the ringwoodite
457 structure, concerning whether it enters only the octahedral or also the tetrahedral site. Neither
458 the UV-VIS nor the MB spectra of the original crystals indicate tetrahedral Fe^{3+} within the
459 resolution of the data. However, analyses of the annealed crystals provide an option for Fe^{3+}
460 in the tetrahedron. The UV-VIS spectrum displays a band around 22000 cm^{-1}, which could be
461 related to either octahedral or tetrahedral Fe^{3+}. Although the energy of the two spin-forbidden
462 bands of tetrahedral Fe^{3+} $^6A_1 \rightarrow {}^4T_1$ and $\rightarrow {}^4T_2$ are expected to be shifted to higher energies

463 compared with similar bands of octahedral Fe^{3+}, the most prominent spin-forbidden transition
464 $^6A_1 \rightarrow {}^4A_1, {}^4E\ (^4G)$, which very likely might be the band at ~22000 cm^{-1}, does not depend on
465 the crystal field strength D_q. Therefore the energy of this transition may be nearly the same
466 for Fe^{3+} in tetrahedral and octahedral coordination (see Burns 1993 pp. 222-223 and Table
467 5.15 for transition band values of octahedral and tetrahedral Fe^{3+} in various minerals). The
468 MB data reveal a similar picture. The spectrum of the annealed ^{57}Fe enriched sample was
469 fitted to different models with no significant difference in the statistical goodness of fit
470 depending on the position of Fe^{3+} doublets. When we assume that all Fe^{2+} and Fe^{3+} is static on
471 the timescale of the Mössbauer effect, the small Fe^{3+}-doublet with lower center shift can be
472 assigned to Fe^{3+} in the tetrahedron. However, in contrast to analyses of the original
473 ringwoodite, both methods show possible evidence for Fe^{3+} in tetrahedral sites in the annealed
474 samples. In fact our assignment of the OH band around 3420 cm^{-1} is based on the presence of
475 cation disorder; thus at least Mg in tetrahedral sites should be present. The shoulder around
476 3420 cm^{-1} in iron-bearing ringwoodite becomes the main band in the spectrum measured after
477 heating and is less enhanced in the spectrum of the annealed Mg endmember. Taking into
478 account the fact that the ferric iron content also rises due to heating, we favor the possibility
479 of Fe^{3+} substituting for silicon in the tetrahedron. Since this process is supplementary to Mg
480 entering tetrahedral sites, the band is more intense than in the pure Mg endmember
481 ringwoodite. We therefore support the idea of tetrahedral Fe^{3+} at least in the annealed
482 samples.

483 In summary, the presence of iron and especially Fe^{3+} in ringwoodite does not appear to
484 influence the total amount of water that is stored in the mineral. In our proposed band
485 assignments we mainly agree with Blanchard et al. (2009) with hydrogen located between O-
486 O pairs of the 16c and 16d octahedral sites (for $[V_{Mg}(OH)_2]^x$) and protonation of tetrahedral
487 edges (for $[Mg/Fe^{2+}/Fe^{3+}{}_{Si}(OH)_2]^x$). However, the broadness of the band around 3150 cm^{-1}
488 indicates that it is a combination of various bands at least due to slightly different O … H

distances which are again due to variable environments and hydrogen disorder as already stated by Panero (2010). Blanchard et al. (2009) also exemplarily chose one additional defect ($[V_{Mg}(OH)_2Mg_{Si}Si_{Mg}]^X$) to calculate its OH frequencies. According to their findings such a defect of hydrogen atoms bound to a vacant Mg-octahedron near to Mg-Si substitution would cause an OH band also located in the range of the broad band around 3150 cm^{-1}. Furthermore we could anticipate that the full width at half maximum (FWHM) of the band is actually increasing with higher Fe content. Thus iron is indeed increasing the number of OH bands in that region. Nevertheless a higher amount of incorporated water due to more possibilities of hydrogen atom locations is not observed in our experiments.

Acknowledgements

We thank Oona Appelt and Dieter Rhede for their help with the electron microprobe analyses and Anja Schreiber who prepared thin foils for TEM. We also gratefully acknowledge the comments and recommendations of A. Beran, an anonymous reviewer and AE B. Mihailova. The work was supported by a grant from the Deutsche Forschungsgemeinschaft (Ko1260/11-1) within the priority program SPP1236.

References cited

Andrut, M., Wildner, M., and Beran, A. (2002) The crystal chemistry of birefringent natural uvarovites. Part IV. OH defect incorporation mechanisms in non-cubic garnets derived from polarized IR spectroscopy. European Journal of Mineralogy, 14, 1019-1026.

Armbruster, T., Kohler, T., Libowitzky, E., Friedrich, A., Miletich, R., Kunz, M., Medenbach, O., and Gutzmer, J. (2001) Structure, compressibility, hydrogen bonding, and dehydration of the tetragonal Mn3+ hydrogarnet, henritermierite. American Mineralogist, 86, 147-158.

Blanchard, M., Balan, E., and Wright, K. (2009) Incorporation of water in iron-free ringwoodite: a fist-principles study. American Mineralogist, 94, 83-89.

Blanchard, M., Wright, K., and Gale, J.D. (2005) Atomistic simulation of Mg_2SiO_4 and Mg_2GeO_4 spinels: A new model. Physics and Chemistry of Minerals, 32, 332-338.

Bolfan-Casanova, N., Keppler, H., and Rubie, D.C. (2000) Water partitioning between nominally anhydrous minerals in the MgO-SiO_2-H_2O system up to 24 GPa: implications for the distribution of water in the Earth´s mantle. Earth and Planetary Science Letters, 182, 209-221.

Burns, R.G. (1993) Mineralogical applications of crystal field theory. Cambridge University Press, 2nd Edition, Cambridge.

Chamorro, P.E.M., Daniel, I., Chervin, J.C., Dumas, P., Bass, J.D., and Inoue, T. (2006) Synchrotron IR study of hydrous ringwoodite γ-Mg_2SiO_4 up to 30 GPa. Physics and Chemistry of Minerals, 33, 502-510.

Deon, F., Koch-Müller, M., Rhede, D., Gottschalk, M., Wirth, R., and Thomas, S.-M. (2010) Location and quantification of hydroxyl in wadsleyite: New insights. American Mineralogist, 95, 312-322.

Hofmeister, A.M., and Mao, H.K. (2001) Evaluation of shear moduli and other properties of silicates with the spinel structure from IR spectroscopy. American Mineralogist, 86, 622-639.

Ingrin, J., and Skogby, H. (2000) Hydrogen in nominally anhydrous upper-mantle minerals: concentration levels and implications. European Journal of Mineralogy, 12, 543-570.

Inoue, T., Weidner, D.J., Northrup, P.A., and Parise, J.B. (1998) Elastic properties of hydrous ringwoodite (γ-phase) in Mg_2SiO_4. Earth and Planetary Science Letters, 160, 107-113.

Inoue, T., Tanimoto, Y., Irifune, T., Suzuki, T., Fukui, H., and Ohtaka, O. (2004) Thermal expansion of wadsleyite, ringwoodite, hydrous wadsleyite and hydrous ringwoodite. Physics of the Earth and Planetary Interiors, 143-144, 279-290.

Kleppe, A.K., Jephcoat, A.P., Smyth, J.R., and Frost, D.J. (2002) On protons, iron and the high-pressure behavior of ringwoodite. Geophysical Research Letters, 29.

Koch-Müller, M., and Rhede, D. (2010) IR absorption coefficients for water in nominally anhydrous high-pressure minerals. American Mineralogist, 95, 770-775.

Koch-Müller, M., Rhede, D., Schulz, R., and Wirth, R. (2009) Breakdown of hydrous ringwoodite to pyroxene and spinelloid at high P and T and oxidizing conditions. Physics and Chemistry of Minerals, 36, 329-341.

Kohlstedt, D.L., Keppler, H., and Rubie, D.C. (1996) Solubility of water in the α, β, and γ phases of $(Mg,Fe)_2SiO_4$. Contributions to Mineralogy and Petrology, 123, 345-357.

Kudoh, Y., Kuribayashi, T., Mizobata, H., and Ohtani, E. (2000) Structure and cation disorder of hydrous ringwoodite, γ-$Mg_{1.89}Si_{0.98}H_{0.30}O_4$. Physics and Chemistry of Minerals, 27, 474-479.

Libowitzky, E. (1999) Correlation of O-H stretching frequencies and O-H. . . O hydrogen bond lengths in minerals. Monatshefte Chemie, 130, 1047-1059.

McCammon, C.A., Frost, D.J., Smyth, J.R., Laustsen, H.M.S., Kawamoto, T., Ross, N.L., and van Aken, P.A. (2004) Oxidation state of iron in hydrous mantle phases: implications for

557 subduction and mantle oxygen fugacity. Physics of the Earth and Planetary Interiors, 143-
558 144, 157-169.
559 Panero, W.R. (2010) First principles determination of the structure and elasticity of hydrous
560 ringwoodite. Journal of Geophysical Research, 115, 1-11.
561 Prescher, C., McCammon, C.A., and Dubrovinsky, L. (2012) MossA - a program for
562 analyzing energy-domain Mossbauer spectra from conventional and synchrotron sources.
563 Journal of Applied Crystallography, 45, 329-331.
564 Prewitt, C.T., and Parise, J.B. (2000) Hydrous Phases and Hydrogen Bonding at High
565 Pressure. Reviews in Mineralogy and Geochemistry, 41, 309-333.
566 Sasaki, S., Prewitt, C.T., Sato, S., and Ito, E. (1982) Single crystal X-ray studies of γ-
567 Mg_2SiO_4. Journal of Geophysical Research, 87, 7829-7832.
568 Schmidt, M.W., and Ulmer, P. (2004) A rocking multianvil; elimination of chemical
569 segregation in fluid-saturated high-pressure experiments. Geochimica et Cosmochimica
570 Acta, 68, 1889-1899.
571 Smyth, J.R., Holl, C.M., Frost, D.J., Jacobsen, S.D., Langenhorst, F., and McCammon, C.A.
572 (2003) Structural systematics of hydrous ringwoodite and water in Earth's interior.
573 American Mineralogist, 88, 1402-1407.
574 Taran, M.N., Koch-Müller, M., Wirth, R., Abs-Wurmbach, I., Rhede, D., and Greshake, A.
575 (2009) Spectroscopic studies of synthetic and natural ringwoodite, γ-$(Mg,Fe)_2SiO_4$.
576 Physics and Chemistry of Minerals, 36, 217-232.
577 van Aken, P.A., and Liebscher, B. (2002) Quantification of ferrous/ferric ratios in minerals:
578 new evaluation schemes of Fe L-23 electron energy-loss near-edge spectra. Physics and
579 Chemistry of Minerals, 29, 188-200.
580 Walker, D. (1991) Lubrication, gasketing, and precision in multianvil experiments. American
581 Mineralogist, 76, 1092-1100.

582 Wirth, R. (2004) A novel technology for advanced application of micro- and nanoanalysis in
583 geosciences and applied mineralogy. European Journal of Mineralogy, 16, 863-876.
584 Ye, Y., Schwering, R.A., and Smyth, J.R. (2009) Effects of hydration on thermal expansion
585 of forsterite, wadsleyite, and ringwoodite at ambient pressure. American Mineralogist,
586 94, 899-904.
587
588
589 Figure Captions
590 Figure 1.
591 Ringwoodite crystal of run MA313 showing its original blue color and acquired green color
592 after the heating cycle up to 500 °C.
593
594 Figure 2.
595 OH-absorption spectra of ringwoodite (MA313) at ambient conditions, 500 °C and after
596 heating. Spectra are offset for clarity. Black lines indicate the OH band maxima (directly read
597 from the spectrum).
598
599 Figure 3.
600 UV-VIS spectra of original ringwoodite (blue) and after annealing at 500 °C (green) and 600
601 °C (orange) of run MA313. Black lines indicate the band assignments (directly read from the
602 spectra).
603
604 Figure 4.
605 MB spectrum of annealed ^{57}Fe enriched ringwoodite (MA327). The two intense doublets with
606 large center shift are assigned to $^{VI}Fe^{2+}$ (in slightly different environments) and the two

607 smaller doublets with lower center shift are due to Fe^{3+} in octahedral (larger area and low QS)
608 and tetrahedral (smaller area and higher QS) sites.
609
610 Figure 5.
611 Band deconvolution plots of the OH-absorption spectra of the original (top) and the annealed
612 (bottom) ringwoodite (MA313) including the five fitted Gaussian and Lorentzian-shaped
613 functions. Peak positions are indicated and represent the maxima of the fitted functions.
614
615 Figure 6.
616 OH-absorption spectra of ringwoodite with different iron contents. Note the shift of the low
617 energy band to higher wavenumbers and vice versa the shift of the high energy band towards
618 lower wavenumbers with increasing x_{Fe}. Spectra are offset for clarity.

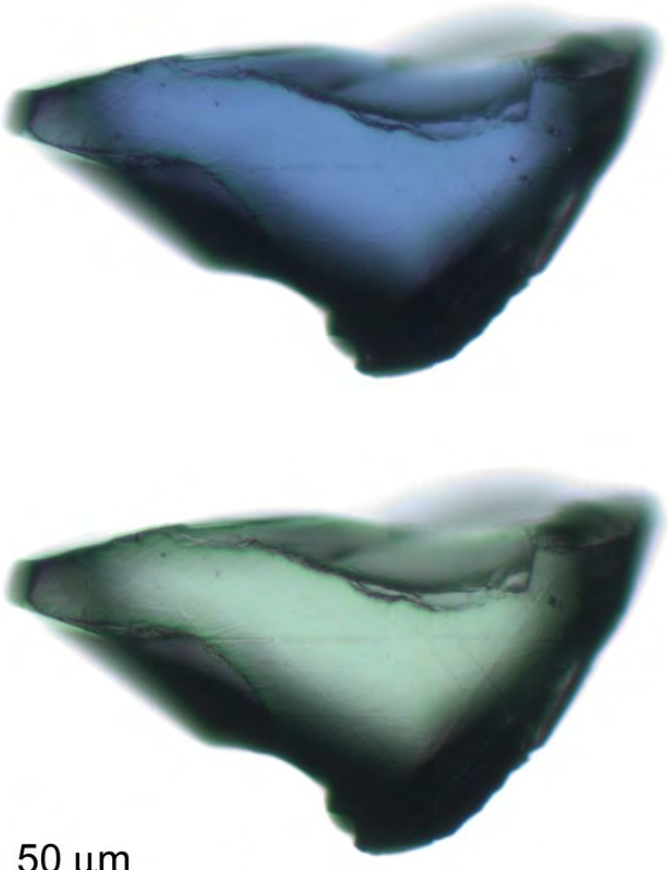
50 µm

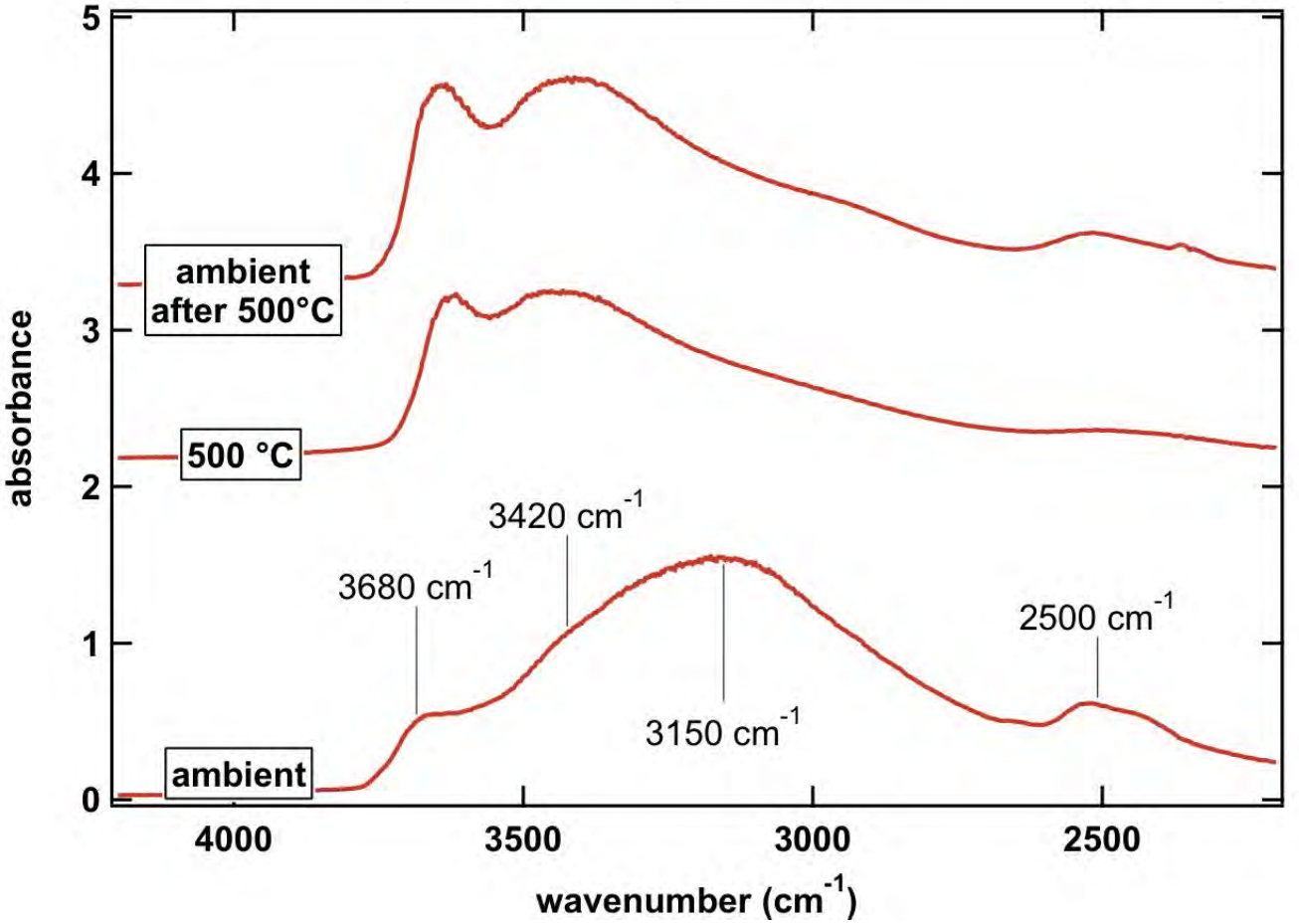
absorbance
wavenumber (cm-1)
ambient after 500°C
500 °C
ambient
3420 cm-1
3680 cm-1
3150 cm-1
2500 cm-1
0
1
2
3
4
5
4000
3500
3000
2500

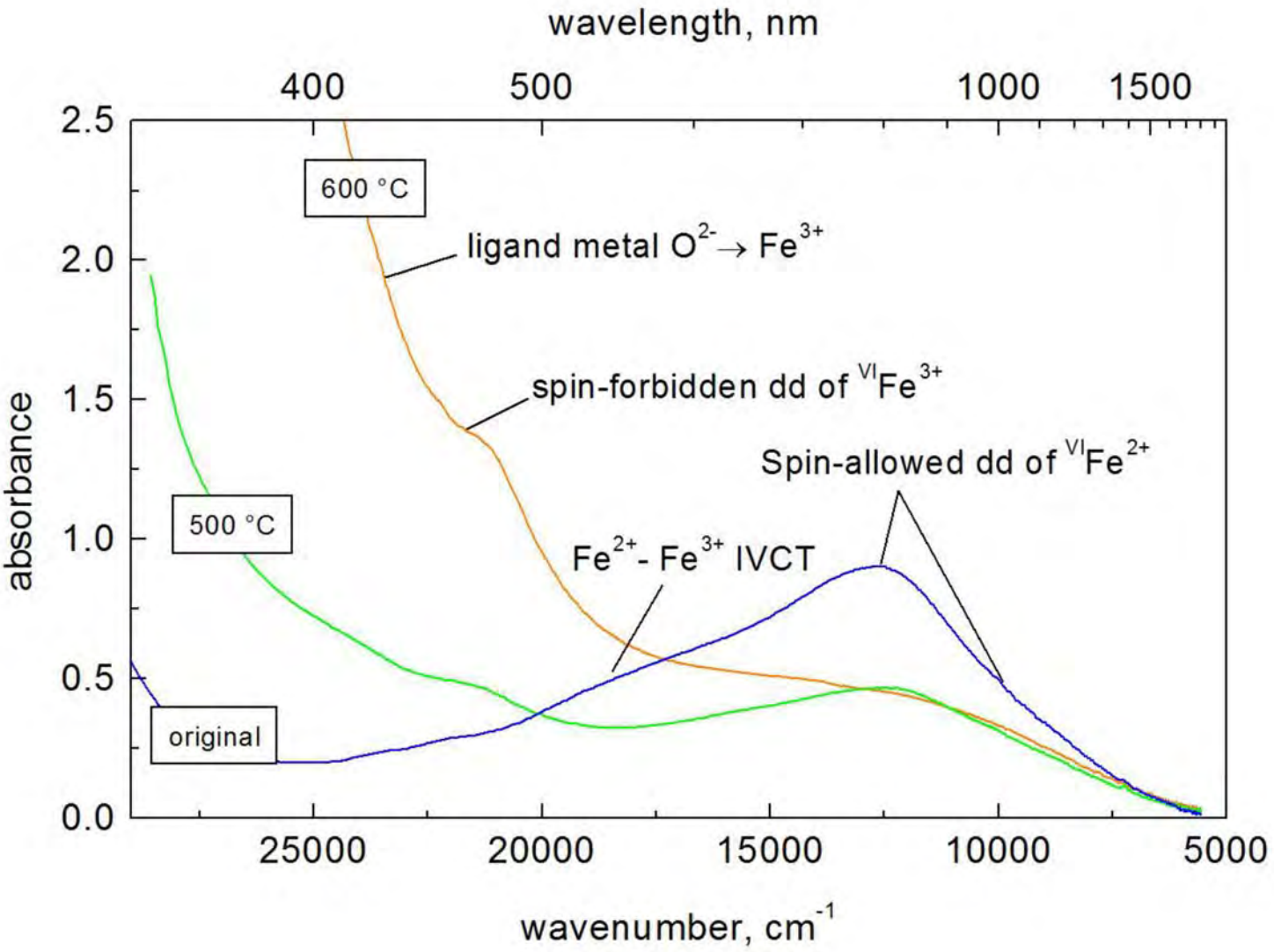
wavelength, nm
400
500
1000
1500
2.5
2.0
1.5
1.0
0.5
0.0
absorbance
600 °C
ligand metal $O^{2-} \rightarrow Fe^{3+}$
spin-forbidden dd of $^{VI}Fe^{3+}$
Spin-allowed dd of $^{VI}Fe^{2+}$
500 °C
Fe^{2+}- Fe^{3+} IVCT
original
25000
20000
15000
10000
5000
wavenumber, cm^{-1}

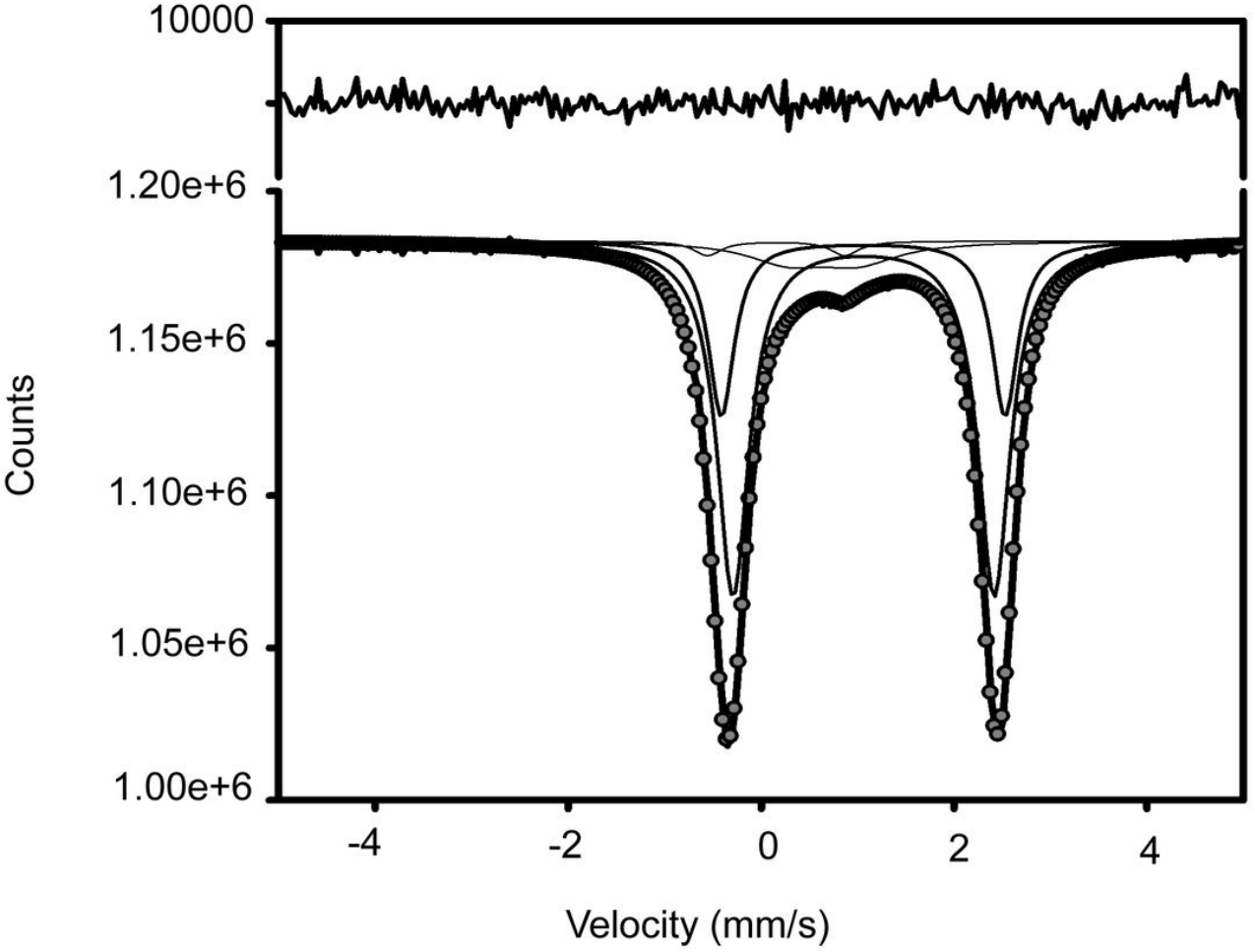
10000
1.20e+6
1.15e+6
1.10e+6
1.05e+6
1.00e+6
Counts
-4
-2
0
2
4
Velocity (mm/s)

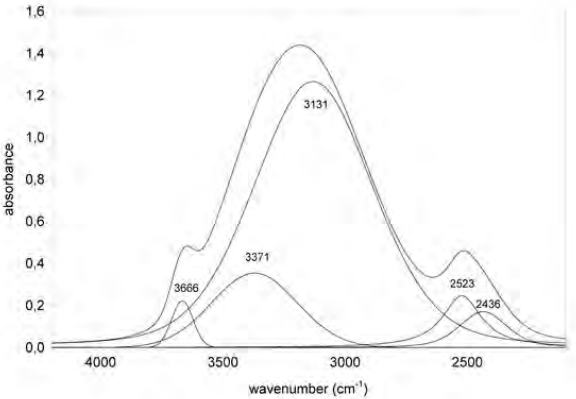
1,6
1,4
1,2
1,0
0,8
0,6
0,4
0,2
0,0
absorbance
3131
3371
3666
2523
2436
4000
3500
3000
2500
wavenumber (cm-1)

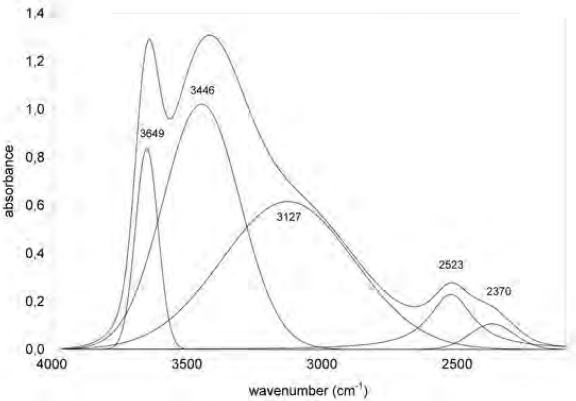
1,4
1,2
1,0
0,8
0,6
0,4
0,2
0,0
absorbance
3446
3649
3127
2523
2370
4000
3500
3000
2500
wavenumber (cm-1)

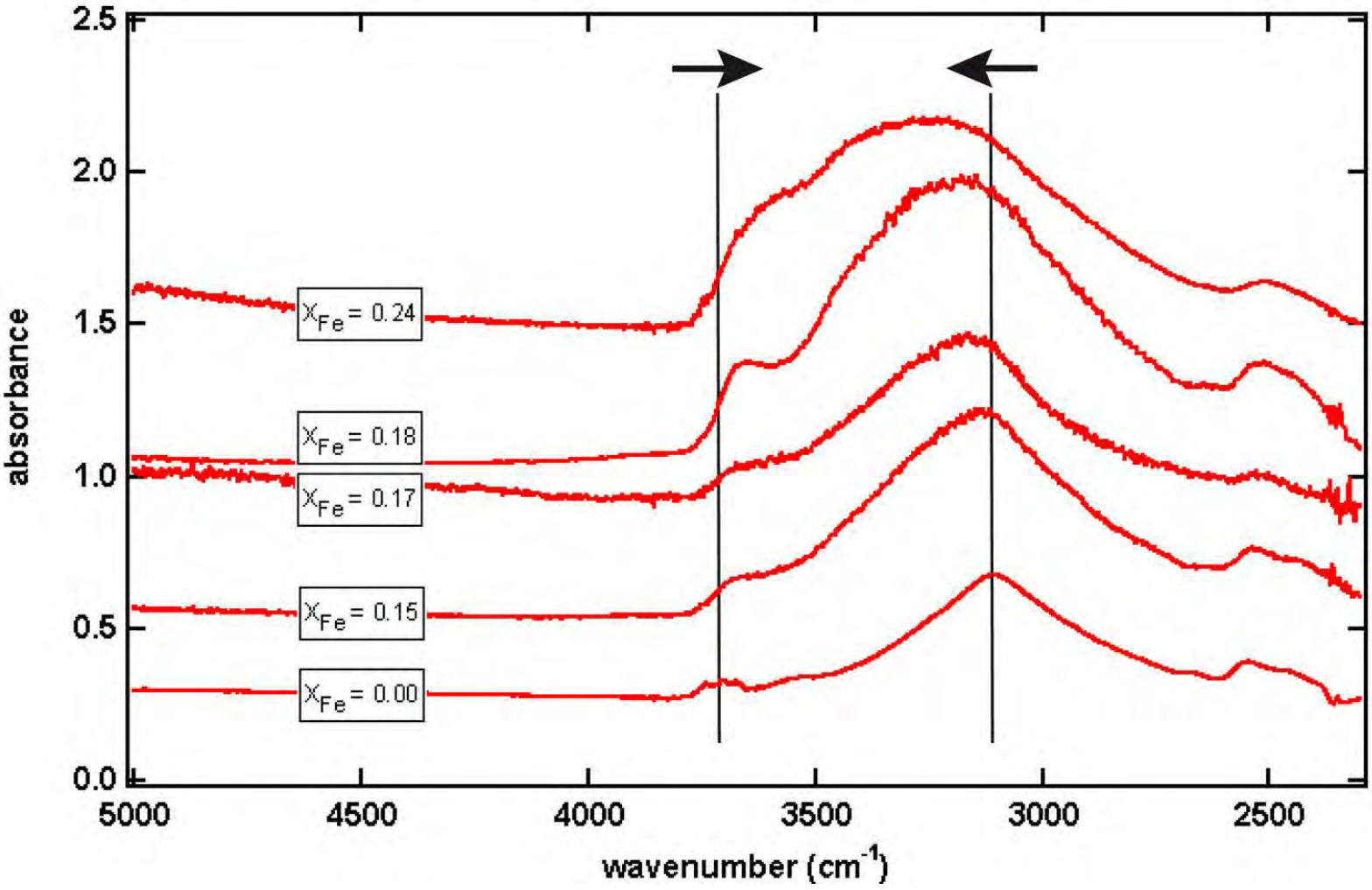
2.5
2.0
1.5
1.0
0.5
0.0
absorbance
X_{Fe} = 0.24
X_{Fe} = 0.18
X_{Fe} = 0.17
X_{Fe} = 0.15
X_{Fe} = 0.00
5000
4500
4000
3500
3000
2500
wavenumber (cm^{-1})

Table 1: Details of run conditions, via FTIR calculated water contents, total iron content x_{Fe}[#] (EMPA), EELS and MB analyses.

run	MA311	MA313	MA327*	MA305	MA308	MA316
P [GPa]	16.5	17.0	18.3	16.7	18.3	17.0
T [°C]	1200	1200	1200	1200	1025 (3h) 975 (6h)	1200
t [h]	4	2	4.5	6	9	4
buffer	Re/ReO_2	Fe/FeO	Re/ReO_2	-	-	-
H_2O [wt.%]	1.2 (2)	1.9 (3)	0.8 (2)	0.8 (2)	0.3 (2)	0.7 (2)
x_{Fe}	0.18 (1)	0.11 (1)	0.24 (1)	0.15 (1)	-	0.18 (1)
Fe^{3+}/Fe_{total} unannealed [%]	10 (3)	6 (3)	EELS: 12 (3) MB: 9 (3)	7 (3)	-	4 (2)
Fe^{3+}/Fe_{total} annealed [%]	-	16 (2)	EELS: 15 (3) MB: 11 (3)	-	-	-

[#] with x_{Fe} corresponding to $(Mg_{1-x}Fe_x)_2SiO_4$
* ^{57}Fe enriched

Table 2: Mössbauer parameters and doublet assignments; the spectrum of the annealed ringwoodite with fitted doublets is given in Fig. 4.

center shift [mm/s]	quadrupole splitting [mm/s]	FWHM [mm/s]	integral area	doublet assignment
original ringwoodite				
1.069	2.767 (01)	0.454 (01)	90.7 (3)	$^{VI}Fe^{2+}$
0.665 (12)	1.063 (22)	0.812 (36)	9.3 (3)	$^{VI}Fe^{3+}$
annealed ringwoodite				
1.082	2.708 (10)	0.403 (03)	63 (3)	$^{VI}Fe^{2+}$
1.077 (01)	2.940 (12)	0.326 (12)	25 (3)	$^{VI}Fe^{2+}$
0.663 (17)	0.729 (27)	1.019 (74)	9.0 (7)	$^{VI}Fe^{3+}$
0.175 (11)	1.425 (24)	0.354 (35)	2.3 (3)	$^{IV}Fe^{3+}$